AIAA JOURNAL
Vol. 49, No. 7, July 2011

Modified Menter Model in Comparison with Recently Developed Single-Equation Turbulence Closures

M. Elkhoury*
Lebanese American University, Byblos, Lebanon

DOI: 10.2514/1.J050648

Five recently developed one-equation turbulence models are assessed against experiments for several flows. These models are the Menter model, modified Menter model, Wu–Nagano model, Fares–Schröder model, and Goldberg model. All models except the latter, which was constructed using physical arguments in boundary layers, were developed using Menter's methodology of transforming two-equation turbulence models to one-equation models using Bradshaw's correlation. The destruction term of the modified Menter model is modified and tested for all considered test cases. This modification renders the model Galilean-invariant and independent of the freestream value of the turbulent intensity. The Spalart–Allmaras turbulence model is also investigated for comparison with the five aforementioned models. Calculations are presented for internal and external flowfields, including zero-pressure-gradient flow over a flat plate, separation and reattachment flows in a backward-facing step, shock/boundary-layer interaction, and adverse-pressure-gradient flows over airfoils at various angles of attack. Although the modified Menter model demonstrates improved predictive capabilities in the majority of the considered cases, its contribution is relatively moderate when compared with existing models.

Nomenclature

A_μ^*, A^+, B_μ	=	turbulence-model closure coefficients
C_f	=	skin-friction coefficient
c_1, c_2, c_3	=	turbulence-model closure coefficients
$c_{\varepsilon 1}, c_{\varepsilon 2}, c_\mu, c_{v1}$	=	turbulence-model closure coefficients
c_{b1}, c_{b2}, c_{w1}	=	turbulence-model closure coefficients
D	=	turbulent destruction, m^2/s^2
$D()/Dt$	=	material derivative
D_1, D_2	=	turbulence-model wall-damping functions
d	=	shortest distance to wall, m
E_{BB}	=	Baldwin–Barth destruction term, m^2/s^2
$\hat{\boldsymbol{F}}, \hat{\boldsymbol{G}}$	=	flux vectors
f_a, f_b, f_e	=	turbulence-model wall-damping functions
$f_{v1}, f_{v2}, f_\varepsilon, f_\mu$	=	turbulence-model wall-damping functions
f_p	=	turbulence-model production limiter
f_β^*, f_β, f_w	=	turbulence-model closure coefficient
g	=	turbulence-model closure coefficient
L_{VK}	=	von Kármán length scale, m
l_r	=	reattachment length, m
P_k	=	turbulence production, m^2/s^2
P^+	=	dimensionless pressure gradient
$\hat{\boldsymbol{Q}}$	=	vector of conserved quantities
$\hat{\boldsymbol{R}}, \hat{\boldsymbol{S}}$	=	viscous flux vectors
Re	=	Reynolds number
r	=	destruction-to-production ratio
S	=	strain-rate magnitude, s^{-1}
S_{ij}	=	strain-rate tensor components, s^{-1}
U, V, W	=	Cartesian mean velocity components, m/s
U_o, V_o, W_o	=	Cartesian reference frame velocity components, m/s
u_e	=	boundary-layer edge velocity
u_ε	=	dimensionless Kolmogorov velocity scale
u^+	=	dimensionless velocity scale
v	=	kinematic viscosity, m^2/s
y_ε	=	dimensionless, Kolmogorov velocity-scaled distance
y^+	=	dimensionless, sublayer-scaled distance
$\alpha, \beta, \beta^*, \beta_c^*$	=	turbulence-model constants
δ^*	=	boundary-layer thickness
ε^*	=	turbulence dissipation rate, m^2/s^3
θ	=	momentum thickness
κ	=	von Kármán constant
$\nu_T, \tilde{\nu}_T$	=	kinematic eddy viscosity, m^2/s
ξ, ζ	=	dimensionless coordinates
σ_R, σ	=	turbulent diffusion coefficient
ϕ	=	test variable for the destruction term, m/s^2
χ	=	turbulent to laminar viscosity ratio
ψ_k	=	dimensionless cross-diffusion function
ψ_ω	=	dimensionless vortex-stretching function
Ω	=	magnitude of the vorticity, s^{-1}
Ω_{ij}	=	vorticity-rate tensor components, s^{-1}

Subscripts

i, j, k	=	Cartesian vector and tensor notation indices
T	=	turbulent
∞	=	freestream

Introduction

OVER the past decade there has been a growing interest in direct numerical simulation (DNS) and large eddy simulation (LES). Although DNS provides accurate prediction and detailed turbulence structure in complex flowfields, it requires high computational resources that are still not practical at high Reynolds numbers. LES is more popular, however, as it demands less computational resources than the DNS and is more accurate than the Reynolds-averaged Navier–Stokes (RANS). Furthermore, the underlying principles behind LES are physically more reasonable than those of the RANS. In spite of these advantages, LES still requires a fine mesh to resolve the filtered large-scale motion, which becomes prohibitive in 3-D complex flows with massive separation at high Reynolds numbers. To remedy this problem, a hybrid RANS/LES approach is currently used in which LES resolves turbulent flow structures away from the

Received 8 May 2010; revision received 11 January 2011; accepted for publication 13 January 2011.

*Department of Industrial and Mechanical Engineering, P.O. Box 36; mkhoury@lau.edu.lb.

wall and RANS is used to model the near-wall turbulence. More accurate approaches that combine both RANS and LES are currently used [1,2], where the LES is locally used to resolve near-wall flow structures in areas where RANS possess weaknesses. Hence, RANS modeling is still essential to accurately account for the near-wall structures of turbulence over complex geometries. Furthermore, solving fewer transport equations is highly desirable to reduce the computational demands, especially when predicting real-world engineering flowfields.

One-equation turbulence models enjoyed a wide popularity, as they are numerically inexpensive, easily implemented, and complete models that directly solve for the eddy viscosity in a flowfield. They are relatively more accurate when compared with standard two-equation models, although they do not account for turbulent time and length scales. One-equation models enjoyed a lengthy history started by Prandtl [3], who derived the k-transport model and related it to the turbulent viscosity via a problem-dependent length scale. Nee and Kovasznay [4], followed by Sekundov [5], were the first to postulate a single-equation model that directly solves for the turbulent viscosity. Baldwin and Barth [6] were among the pioneers who derived their one-equation model by transforming the classical k-ε closure. Their model performed very differently when compared with its parent k-ε model, however, even in simple equilibrium flows [7]. To a large extent, the failure of the Baldwin–Barth (BB) turbulence model was due to the assumptions made in the transformation process, which led to ill-conditioned behavior near turbulent/nonturbulent interfaces [7]. The BB model was closely followed by the Spalart–Allmaras (SA)[8] model, which has been among the most popular and widely used models. Unlike the BB model, the SA model was developed from physical arguments in wall-bounded and free-shear flows. The main disadvantage of this model is its explicit wall dependency rendering it inflexible. Later, Menter [7] demonstrated an approach in which two-equation closures could be transformed to one-equation models using Bradshaw's relation. The resultant model showed a closer bond to its parent k-ε model when compared with the BB closure. Goldberg [9,10] developed two one-equation models that are similar to the BB model in the high-Reynolds-number form, except that the destruction term was conditioned near boundary-layer edges, which is an approach aimed to eliminate what the BB model inherited from the use of such a destruction term. However, this condition rendered both models non-Galilean-invariant. Nagano et al. [11], and Fares and Schröder [12] derived their one-equation models using Menter's strategy. Nagano et al. [11] transformed the low-Reynolds-number k-ε model, which resulted in many nonlinear and mostly singular wall-reflecting terms. To remedy this problem, Wu and Nagano [13] simplified their original model by eliminating these terms that negatively influenced the stability and the convergence of the numerical simulations. Furthermore, they adjusted the model's constants and wall functions and tested it in channel and boundary-layer flows with and without pressure gradients. Fares and Schröder [12] transformed Wilcox's [14] two-equation k-ω model and showed good results in wall-bounded and free-shear flows. Elkhoury [15] modified Menter's model by limiting the production rate and assessed the performance of the model with different destruction terms using Goldberg's [9,10] proposed modification to the destruction term. Elkhoury [16] proposed a one-equation model based on the transformation of the k-ε model that included the Yap correction term and applied it to several aerodynamic flows.

Galilean invariance is an important criterion for all turbulent models to possess, especially when multiple moving boundaries are present. Hence, the first objective of the present work is to modify the destruction term of the one-equation k-ω-based Menter model [15] by eliminating Goldberg's [9,10] condition and hence rendering the model Galilean-invariant. Furthermore, the proposed modification results in a model that is insensitive to the freestream values of the turbulent intensity.

The second objective is to test the predictive capabilities of five newly developed single-equation turbulence models. These models were not validated beyond the scientific journals in which they were postulated, providing another incentive behind this work. The SA model is also included to serve as a benchmark against which other models will be assessed. All six one-equation turbulence models are carefully assessed throughout flow computations over several challenging test cases. Velocity profiles, turbulent shear stresses, and skin-friction coefficients are numerically simulated and assessed against theoretical/experimental data.

Investigated Turbulence Models

The six turbulence models that have been assessed in this work are as follows.

Fares–Schröder Model

Fares and Schröder (FS) [12] transformed the refined k-ω two-equation turbulence closure of Wilcox [14] using Menter's [7] methodology to a one-equation model. The final form of the model excluding the isentropic decay of turbulence term can be expressed as

$$\frac{\mathrm{D}\tilde{\nu}_T}{\mathrm{D}t} = \underbrace{2(1-\alpha)\sqrt{\beta_c^*}\frac{\tilde{\nu}_T}{S}S_{ij}\frac{\partial u_i}{\partial x_j}}_{\text{production}} + \underbrace{\frac{\partial}{\partial x_j}\left((\nu+\sigma\tilde{\nu}_T)\frac{\partial\tilde{\nu}_T}{\partial x_j}\right)}_{\text{diffusion}} - \underbrace{\frac{(\beta^*-\beta)}{\sqrt{\beta_c^*}}\tilde{\nu}_T S}_{\text{destruction}} + \underbrace{2\frac{(\nu+\sigma\tilde{\nu}_T)}{S}\frac{\partial\tilde{\nu}_T}{\partial x_j}\frac{\partial S}{\partial x_j}}_{\text{destruction/diffusion}} \tag{1}$$

The functions ψ_k and ψ_ω (and, consequently, f_β^* and f_β) account for the cross-diffusion and vortex-stretching [14] and follow from the transformation of Wilcox model:

$$\beta^* = \beta_c^* f_\beta^*, \qquad f_\beta^* = \frac{1+650\psi_k}{1+100\psi_k}$$

$$\psi_k = \max\left[0., \frac{\sqrt{\beta_c^*}}{S^3}\left(\nu_T\left(\frac{\partial S}{\partial x_j}\right)^2 + S\frac{\partial\nu_T}{\partial x_j}\frac{\partial S}{\partial x_j}\right)\right] \tag{2}$$

$$\beta = \beta_c f_\beta, \qquad f_\beta = \frac{1+70\psi_\omega}{1+80\psi_\omega}, \qquad \psi_\omega = \left|\frac{\Omega_{ij}\Omega_{jk}S_{ki}}{(\sqrt{\beta_c^*}S)^3}\right| \tag{3}$$

where $S = \sqrt{2S_{ij}S_{ij}}$, $S_{ij} = (\partial U_i/\partial x_j + \partial U_j/\partial x_i)/2$, and $\Omega_{ij} = (\partial U_i/\partial x_j - \partial U_j/\partial x_i)/2$.

It is worth noting that the cross-diffusion function was included in the model to solely account for free-shear flows, whereas the vortex-stretching function is zero for two-dimensional flows. The near-wall-damping function of Mellor and Herring [17] was used to damp the eddy viscosity:

$$f_{v1} = \frac{\chi^3}{c_{v1}^3+\chi^3}, \qquad \chi = \frac{\tilde{\nu}_T}{\nu}, \qquad \nu_T = \tilde{\nu}_T f_{v1} \tag{4}$$

Preliminary test cases of the one-equation model based on k-ω closure performed by Menter [7] revealed the dependency of the model on the freestream value of the eddy viscosity. This means that the model carried this deficiency from its parent k-ω model. Furthermore, large gradients in velocities develop near the boundary-layer edge, which was possibly attributed to the low value of diffusion coefficient. To eliminate these deficiencies, the model's constants σ and α were recalibrated [12]. The coefficients of the model are

$$\alpha = 0.29, \qquad \sigma = 1.2, \qquad \beta_c^* = 0.09$$
$$\beta_c = 0.072, \qquad c_{v1} = 9.1 \tag{5}$$

Wu–Nagano Model

The Wu–Nagano (WN) model was originally derived by Nagano et al. [11] via the transformation of the low-Reynolds-number (LRN) k-ε model [18] to a LRN one-equation model. No damping functions were pragmatically imposed on the model as near-wall terms were explicitly demonstrated in their model. However, these terms were

singular and highly nonlinear in the near vicinity of the wall [13]. Furthermore, the near-wall terms were so many that their implementation was very difficult and had negative influence on the stability and convergence of the numerical solution rendering the model less attractive. Wu and Nagano [13] proposed another version where they simplified the model by amending theses terms and adjusting its constants and functions. The modified model, which reproduces correct wall-limiting behavior of turbulence, was tested for boundary-layer flows with and without adverse pressure gradients and for channel flows at various Reynolds numbers [13]. The simplified model is summarized as follows:

$$\frac{\mathrm{D}\nu_T}{\mathrm{D}t} = \underbrace{c_1 \nu_T S}_{\text{production}} + \underbrace{\frac{\partial}{\partial x_j}\left(\left(\nu + \frac{\nu_T}{\sigma}\right)\frac{\partial \nu_T}{\partial x_j}\right)}_{\text{diffusion}} - \underbrace{c_3 E_{\mathrm{BB}} \tanh\left[\frac{2(\nu + \nu_T/\sigma)\nu_T((\partial S/\partial x_j)/S)^2}{c_3 E_{\mathrm{BB}}}\right]}_{\text{destruction}} \tag{6}$$

where E_{BB} is the Baldwin–Barth's destruction term used as an upper bound and is given by

$$E_{\mathrm{BB}} = \frac{\partial \nu_T}{\partial x_j}\frac{\partial \nu_T}{\partial x_j} \tag{7}$$

The production's term c_1 coefficient can be expressed as

$$c_1 = \sqrt{C_\mu f_a}[(2 - c_{\varepsilon 1}) + (c_{\varepsilon 2} f_\varepsilon - 2) f_b] \tag{8}$$

with the following wall functions:

$$f_\mu = [1 - e^{-y_\varepsilon / A_\mu^*}]^2\left(1 + \frac{B_\mu}{y_\varepsilon^3}\right), \qquad f_a = [1 - e^{-(y_\varepsilon/18)^6}]^{1/3} \tag{9}$$

The coefficients B_μ and A_μ^* are given by

$$B_\mu = 20.3 \times Re_\infty^{1/7}, \qquad A_\mu^* = 16/[1 + 63P^+] \tag{10}$$

where Re_∞ is based on the freestream Reynolds number and the nondimensional pressure follows as $P^+ = \nu(\mathrm{d}P/\mathrm{d}x)/(\rho u_\tau^3)$. Here, y_ε is a nondimensional distance from the wall that is based on the Kolmogorov velocity scale $u_\varepsilon = (\nu\varepsilon^*)^{1/4}$, since basing it on the friction velocity might lead to absurd results in flows that involve separation and reattachment. The nondimensional distance can be defined by

$$y_\varepsilon = u_\varepsilon y/\nu \tag{11}$$

A corrected definition of the dissipation rate, ε^* is given by

$$\varepsilon^* = f_b \nu_T S^2 + \varepsilon_a, \quad \text{with} \quad f_b = \frac{f_\mu}{f_a} \tag{12}$$

where ε_a corrects the dissipation rate away from the wall and is given by

$$\varepsilon_a = 0.6 f_e[\sqrt{\bar{U}_i^2/2}/(1 + \nu_T/\nu)]^4/\nu, \quad \text{with} \quad f_e = 1 - e^{-(\nu_T/35\nu)^3} \tag{13}$$

with the following constants:

$$c_{\varepsilon 1} = 1.45, \qquad c_{\varepsilon 2} = 1.9, \qquad c_3 = 7.0$$
$$c_\mu = 0.09, \quad \text{and} \quad \sigma = 1.8 \tag{14}$$

The main shortcoming of this model lies in its dependency on the nonlocal flow variables such as the freestream velocity, which is outside the boundary layer.

Goldberg Model

Goldberg [9] developed a one-equation model for the eddy viscosity that is similar to the BB model in the high-Reynolds-number form. The model was calibrated using physical argument in turbulent boundary layer. The transport equation, which is wall-distance-free, can be expressed as

$$\frac{\mathrm{D}\tilde{\nu}_T}{\mathrm{D}t} = \underbrace{c_1(\tilde{\nu}_T P_k)^{1/2}}_{\text{production}} + \underbrace{\frac{\partial}{\partial x_j}\left(\left(\nu + \frac{\tilde{\nu}_T}{\sigma_R}\right)\frac{\partial \tilde{\nu}_T}{\partial x_j}\right)}_{\text{diffusion}} - \underbrace{(c_3 f_3 - c_2)D}_{\text{destruction}} \tag{15}$$

The turbulence production, expressed in terms of the Boussinesq model, is given by

$$P_k = \nu_t\left[\left(\frac{\partial U_i}{\partial x_j} + \frac{\partial U_j}{\partial x_i}\right)\frac{\partial U_i}{\partial x_j} - \frac{2}{3}\left(\frac{\partial U_k}{\partial x_k}\right)^2\right] \tag{16}$$

and the destruction term is given by

$$D = \begin{cases} \frac{\partial \tilde{\nu}_T}{\partial x_j}\frac{\partial \tilde{\nu}_T}{\partial x_j} & \text{if } \phi > 0, \\ 0, & \text{Otherwise} \end{cases} \tag{17}$$

where

$$\phi = \frac{\partial V_{\mathrm{Total}}}{\partial x_j}\frac{\partial \tilde{\nu}_T}{\partial x_j}$$
$$V_{\mathrm{Total}} = [(U - U_0)^2 + (V - V_0)^2 + (W - W_0)^2]^{1/2} \tag{18}$$

Here, U_0, V_0, and W_0 are the reference-fame velocities taken here as zero. This condition is usually active near shear-layer edges, thus avoiding sharp turbulence/nonturbulence interface. The damped eddy viscosity is defined by

$$\nu_T = f_\mu \tilde{\nu}_T \tag{19}$$

where the damping functions are given by

$$f_\mu = [\tanh(\alpha\chi^2)]/[\tanh(\beta\chi^2)], \qquad f_3 = 1 + 2\alpha/(3\beta c_3\chi)$$
$$\chi = \tilde{\nu}_T/\nu \tag{20}$$

with the following constants:

$$c_2 = -5\alpha/(3\beta c_3\chi), \qquad c_1 = \kappa^2(c_3 - c_2 - \sigma_R^{-1})$$
$$c_3 - c_2 = 3/(2\sigma_R), \qquad \sigma_R = 0.8, \qquad \alpha = 0.07, \qquad \beta = 0.2 \tag{21}$$

Menter Model

Menter derived this model from the transformation of the k-ε two-equation model using Bradshaw's hypothesis. The main difference between the BB and the present model lies in the form of the destruction term where the latter is based on the inverse of the von Kármán mixing length scale. It is worth noting that other models such as the one by Durbin et al. [19] use this length scale, however, without deriving it from the k-ε closure. The transport equation for the eddy viscosity is as follows:

$$\frac{\mathrm{D}\tilde{\nu}_T}{\mathrm{D}t} = \underbrace{D_1 c_1 \Omega \tilde{\nu}_T}_{\text{production}} + \underbrace{\frac{\partial}{\partial x_j}\left(\left(\nu + \frac{\tilde{\nu}_T}{\sigma}\right)\frac{\partial \tilde{\nu}_T}{\partial x_j}\right)}_{\text{diffusion}} - \underbrace{c_2 c_3 \min\left(\frac{\tilde{\nu}_T^2}{c_3 L_{\mathrm{VK}}^2}, \left(\frac{\partial \tilde{\nu}_T}{\partial x_j}\right)^2\right)}_{\text{destruction}} \tag{22}$$

The inverse of the von Kármán length scale can be expressed as

$$\frac{1}{L_{\mathrm{VK}}^2} \to \left[\left(\frac{\partial \Omega}{\partial x_j}\frac{\partial \Omega}{\partial x_j}\right)\Big/\Omega^2\right] \tag{23}$$

where $\Omega = \sqrt{\Omega_{ij}\Omega_{ij}}$, and the eddy viscosity is given by

$$\nu_T = \tilde{\nu}_T D_2 \tag{24}$$

with the following damping functions:

$$D_1 = \frac{\nu_T + \nu}{\tilde{\nu}_T + \nu}, \qquad D_2 = 1 - e^{-(\tilde{\nu}_T/A^+\kappa\nu)^2} \tag{25}$$

The model's coefficients follow directly from the transformation of the k-ε model:

$$c_1 = 0.144, \qquad c_2 = 1.86, \qquad c_3 = 7.0$$
$$\sigma = 1.0, \qquad A^+ = 13, \qquad \kappa = 0.41 \tag{26}$$

Modified Menter Model

Elkhoury [15] modified Menter's one-equation model primarily by limiting the production rate and thus improving the model's predictive capabilities in nonequilibrium flows while retaining its performance in simple boundary-layer flows. The modified version of the k-ω-based one-equation model is given by

$$\frac{\mathrm{D}\tilde{\nu}_T}{\mathrm{D}t} = \underbrace{f_p D_1 c_1 \Omega \tilde{\nu}_T}_{\text{production}} + \underbrace{\frac{\partial}{\partial x_j}\left(\left(\nu + \frac{\tilde{\nu}_T}{\sigma}\right)\frac{\partial \tilde{\nu}_T}{\partial x_j}\right)}_{\text{diffusion}} - \underbrace{c_2 D}_{\text{destruction}} \tag{27}$$

The production limiter, which is similar to the one used in Elkhoury [15], is given by

$$f_p = \min(1.0, \max(r^{0.03}, e^{-\tilde{\nu}_T/200\nu})) \tag{28}$$

where r is the destruction-to-production ratio given by

$$r \equiv \frac{|\frac{\partial \tilde{\nu}_T}{\partial x_j}|}{S\kappa^2 L_{\mathrm{VK}}} \tag{29}$$

The exponent term $e^{-\tilde{\nu}_T/\nu 200}$ in the f_p limiter was introduced to eliminate any transition effect that the destruction-to-production ratio, r, might have on the turbulence model. To demonstrate this, the steady incompressible boundary-layer equation for two-dimensional flow for the kinematic eddy viscosity, without viscous damping, can be used and written as

$$U\frac{\partial \tilde{\nu}_T}{\partial x} + V\frac{\partial \tilde{\nu}_T}{\partial y} = P_{\tilde{\nu}_T} c_2 \frac{\tilde{\nu}_T}{L_{\mathrm{VK}}}\left|\frac{\partial \tilde{\nu}_T}{\partial y}\right| + \frac{\partial}{\partial y}\left(\left(\nu + \frac{\tilde{\nu}_T}{\sigma}\right)\frac{\partial \tilde{\nu}_T}{\partial y}\right) \tag{30}$$

where the production-per-unit-destruction term can be formulated as follows:

$$P_{\tilde{\nu}_T} = \left(\frac{c_1 \partial U/\partial y L_{\mathrm{VK}}}{c_2 |\partial \tilde{\nu}_T/\partial y|} - 1\right) \tag{31}$$

The sign of $P_{\tilde{\nu}_T}$ determines whether $\tilde{\nu}_t$ amplifies or reduces in magnitude. Using the Blasius similarity variable defined by $\eta = y/\sqrt{\nu x/U_\infty}$, a dimensionless velocity $U = U_\infty U(x, \eta)$ along with a scaling of $\nu N(x, \eta)$ for the eddy viscosity $\tilde{\nu}_t$, show that $P_{\tilde{\nu}_T}$ varies with Reynolds number, or

$$P_{\tilde{\nu}_T} = \left(\frac{c_1 \sqrt{Re_x}(\partial U/\partial \eta)^2}{c_2 |\partial^2 U/\partial \eta^2||\partial N/\partial \eta|} - 1\right) \tag{32}$$

For a flat-plate boundary layer, at some distance downstream the leading when $P_{\tilde{\nu}_T} > 0$ the eddy viscosity grows rapidly and transition to turbulence takes place. To facilitate the analysis, let

$$X = \frac{\sqrt{Re_x}(\partial U/\partial \eta)^2}{|\partial^2 U/\partial \eta^2||\partial N/\partial \eta|}$$

and using $c_1 = 0.144$, $c_2 = 1.86$ $P_{\tilde{\nu}_T} > 0$ when $X > 12.92$. With the current modification to the production term Eq. (32) can be expressed as

$$P_{\tilde{\nu}_T} = \left(\frac{c_1 X}{c_2 \kappa^{2n} X^n} - 1\right) \tag{33}$$

where the destruction-to-production ratio defined by Eq. (29) is written as, $r^n = 1/(\kappa^{2n} X^n)$. It is clear that with $n = 0.03$ and $\kappa = 0.41$, $P_{\tilde{\nu}_T} > 0$ when $X > 13.2$, which means that transition will take place further downstream, when compared with the original model's predictions. To retain the same transition location of the original model the exponent $e^{-\tilde{\nu}_T/\nu 200}$ was introduced. It is worth noting that around the transition location, $\tilde{\nu}_t$ is of the same order of magnitude as that of the laminar kinematic viscosity ν; thus, $e^{-\tilde{\nu}_T/\nu 200} \to 1$ and, as a result, $f_p \to 1$. The constant in the exponent was found numerically, such that the MM model does not alter the transition location predicted by the original ME model. Figure 1 shows a comparison of predicted skin-friction coefficient over a flat plate for the ME model and the MM model, including and excluding the exponent term $e^{-\tilde{\nu}_T/\nu 200}$. Hence, it clear that with the inclusion of this term, the f_p limiter does not alter the transition location of the original ME model.

Models with destruction terms

$$\frac{\partial \tilde{\nu}_T}{\partial x_j}\frac{\partial \tilde{\nu}_T}{\partial x_j}$$

and

$$\frac{\tilde{\nu}_T}{c_3 L_{\mathrm{VK}}}|\frac{\partial \tilde{\nu}_T}{\partial x_j}|$$

are sensitive to freestream values of turbulent viscosity and produce high-velocity gradients near boundary-layer edges [7]. To remedy this, Elkhoury [15] adopted Goldberg's [9,10] approach in treating the destruction term of the above model, i.e.,

$$D = \frac{\tilde{\nu}_T}{c_3 L_{\mathrm{VK}}}\left|\frac{\partial \tilde{\nu}_T}{\partial x_j}\right| \text{if } \phi > 0$$

and $D = 0$ otherwise. Although this modification works perfectly near boundary-layer edges where $\phi < 0$, it renders the model non-Galilean-invariant, and becomes problematic with multiple moving walls.

Proposed Modification to the Destruction Term

In his 2006 version of the k-ω model, Wilcox [20] added a cross-diffusion term

$$\frac{\partial k}{\partial x_j}\frac{\partial \omega}{\partial x_j}$$

to the ω equation that is active near shear-layer edges and in free-shear flows, causing the model to behave like the k-ε closure. To achieve this, Wilcox [20] added this term only when

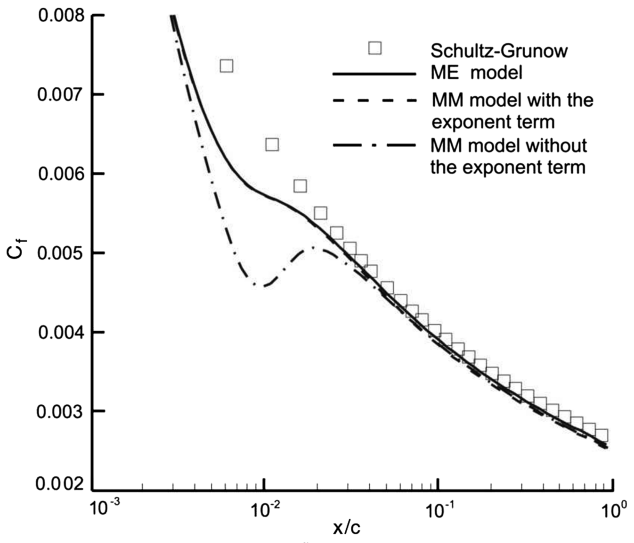

Fig. 1 Effect of the exponent, $e^{-\tilde{\nu}_T/\nu 200}$ on the transition location for a flow over a flat plate.

$$\frac{\partial k}{\partial x_j}\frac{\partial \omega}{\partial x_j} > 0$$

and neglected it near solid boundaries, where

$$\frac{\partial k}{\partial x_j}\frac{\partial \omega}{\partial x_j} \le 0$$

Hence, based on its sign, the model retains its original k-ω formulation in near-wall regions and shifts to k-ε near shear-layer edges. This condition is transformed to the k-ω-based one-equation model using Bradshaw's hypothesis $\nu_T\Omega = \sqrt{C_\mu k}$ and the kinematic eddy viscosity $\nu_t = k/\omega$. The following relation follows from this transformation:

$$\phi = \frac{\partial \Omega}{\partial x_j}\frac{\partial \tilde{\nu}_T}{\partial x_j}\Omega + \tilde{\nu}_T\frac{\partial \Omega}{\partial x_j}\frac{\partial \Omega}{\partial x_j} \tag{34}$$

It is worth noting that the first term is always ≤ 0 in the inner part of the boundary layer and is >0 in the outer part when both, the vorticity and the eddy viscosity rates decrease toward the shear-layer edge. For a boundary-layer flow over a flat plate $\partial U/\partial y$ is constant and is equal to u_τ/ν in the viscous sublayer, which implies that $\phi = 0$. Substituting $\partial(\partial U/\partial y)/\partial y = -u_\tau\kappa/y^2$ and $\partial \nu_t/\partial y = u_t\kappa$ into Eq. (34) for the logarithmic-layer result $\sin\phi = 0$. As $\partial\tilde{\nu}_T/\partial y$ starts to decrease in the outer part of the boundary layer, $\phi \to >0$ and the destruction term shifts to that of the k-ε-based model. Furthermore, it is easily verified that the destruction terms of both the k-ω- and k-ε-based models can be obtained when Eq. (34) is multiplied by $\tilde{\nu}_t/\Omega^2$. It is clear from previous work [7,12] that the destruction term of the k-ω-based model is almost always negative and larger in magnitude than that of the k-ε-based model. Thus, ϕ is almost always ≤ 0, except for the outer part of the boundary layer when $\partial\tilde{\nu}_t/\partial y < 0$. The proposed destruction term can be expressed as

$$D = \begin{cases} \dfrac{\tilde{\nu}_T^2}{L_{\mathrm{VK}}^2} & \text{if } \phi > 0 \\ \dfrac{\tilde{\nu}_T}{L_{\mathrm{VK}}}\left|\dfrac{\partial \tilde{\nu}_T}{\partial x_j}\right| & \text{otherwise} \end{cases} \tag{35}$$

The model's coefficients and damping functions are the same as those of the ME model, except that $A^+ = 12$ for the present model. Furthermore, the destruction-to-production ratio, r, should also shift to that of the k-ε-based one-equation model whenever $\phi > 0$, i.e.,

$$r = \begin{cases} \dfrac{\tilde{\nu}_T}{S\kappa^2 L_{\mathrm{VK}}^2} & \text{if } \phi > 0 \\ \dfrac{|(\partial\tilde{\nu}_T/\partial x_j)|}{S\kappa^2 L_{\mathrm{VK}}} & \text{otherwise} \end{cases} \tag{36}$$

The implementation of this destruction term eliminates the sensitivity of the model to freestream values of turbulence viscosity. Figure 2 shows the variation of $y/\delta_{0.99}$ vs $\nu_T/(u_e\delta^*)$ for, respectively, the k-ω-based single-equation model with the unmodified destruction term,

$$\frac{\tilde{\nu}_T}{c_3 L_{\mathrm{VK}}}\left|\frac{\partial \tilde{\nu}_T}{\partial x_j}\right|$$

and with the present modification. It can be clearly deduced that the unmodified k-ω-based one-equation model demonstrates sensitivity to high and low freestream values of turbulent viscosity. However, the present modification eliminates this sensitivity and renders the model Galilean-invariant.

Spalart–Allmaras Model

This model, which was derived from physical arguments in boundary layers and free-shear flows, is mature and well verified in literature. The SA model excluding the transition terms can be written as

$$\frac{\mathrm{D}\tilde{\nu}_T}{\mathrm{D}t} = \underbrace{c_{b1}\tilde{\Omega}\tilde{\nu}_T}_{\text{production}} + \underbrace{\frac{\partial}{\partial x_j}\left(\frac{(\tilde{\nu}_T + \tilde{\nu})}{\sigma}\frac{\partial \tilde{\nu}_T}{\partial x_j}\right) + c_{b2}\left(\frac{\partial \tilde{\nu}_T}{\partial x_j}\right)^2}_{\text{diffusion}} - \underbrace{c_{w1}f_w\left(\frac{\tilde{\nu}_T}{d}\right)^2}_{\text{destruction}} \tag{37}$$

The modified magnitude of vorticity is given by

$$\tilde{\Omega} = \Omega + \frac{\tilde{\nu}_T}{\kappa^2 d^2}f_{v2} \tag{38}$$

The closure coefficients and damping functions are as follows:

$$g = r + c_{w2}(r^6 - r), \qquad c_{w1} = \frac{c_{b1}}{\kappa^2} + \frac{(1 + c_{b2})}{\sigma} \tag{39}$$

$$f_{v2} = 1 - \frac{\chi}{1 + \chi f_{v1}}, \qquad \chi = \frac{\tilde{\nu}_T}{\nu}, \qquad f_{v1} = \frac{\chi^3}{c_{v1}^3 + \chi^3} \tag{40}$$

$$f_w = g\left[\frac{1 + c_{w3}^6}{g^6 + c_{w3}^6}\right]^{1/6}, \qquad r = \frac{\tilde{\nu}_T}{\tilde{\Omega}\kappa^2 d^2} \tag{41}$$

$$c_{b1} = 0.1355, \qquad c_{b2} = 0.622, \qquad c_{v1} = 7.1$$
$$c_{w2} = 0.3, \qquad \sigma = 2/3 \tag{42}$$

and the damped eddy viscosity is given by

$$\nu_T = \tilde{\nu}_T f_{v1} \tag{43}$$

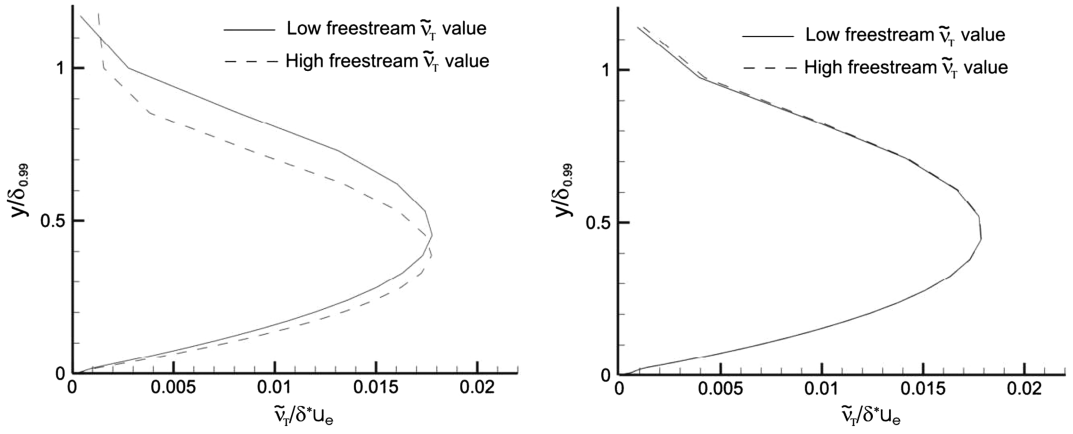

Fig. 2 Effect of freestream turbulence intensity on the viscosity for the original and the modified one-equation k-ω-based model.

Numerical Method

An unsteady, implicit, compressible/incompressible full Navier–Stokes solver was employed in curvilinear coordinate system (ξ, ζ). The governing equations are given by

$$\partial_t \hat{\mathbf{Q}} + \partial_\xi \hat{\mathbf{F}} + \partial_\zeta \hat{\mathbf{G}} = Re^{-1}(\partial_\xi \hat{\mathbf{R}} + \partial_\zeta \hat{\mathbf{S}}) \tag{44}$$

Here, $\hat{\mathbf{Q}}$ is the vector of conserved variables $1/J(\rho, \rho u, \rho w, e)$, $\hat{\mathbf{F}}$ and $\hat{\mathbf{G}}$ are the convection flux vectors, and $\hat{\mathbf{R}}$ and $\hat{\mathbf{S}}$ are the viscous fluxes in the ξ and ζ directions along, respectively, the axial and normal to a solid boundary. The solver features a third-order-accurate Osher's upwind-biased flux difference splitting scheme. The viscous fluxes are computed with second-order-accurate central differences. All models are solved and decoupled using an implicit approximate factorization method. Further details regarding the numerical implementation are available in [8,21,22].

Results and Discussion

Five different test cases were used for the assessment and validation of all the considered turbulence models. The first case is flow over a flat plate with zero pressure gradient. The second test case involves a shock/boundary-layer interaction over the NACA 0012 airfoil. The third and fourth test cases involve adverse pressure gradient over the Aerospatiale-A airfoil and the NACA 4412, respectively. The fifth and last test case is the backward-facing-step flow that involves separation at a relatively low pressure gradient. A C-type grid was used for all airfoil test cases. For all external-flow test cases, the freestream turbulent eddy viscosity is set to one tenth of the laminar eddy viscosity and the inflow/outflow boundary variables are evaluated using Riemann-invariant extrapolation. A grid study was conducted for all test cases to ensure grid independence. The complexity of all the models' functions had no effect on the numerical stability of the computations resulting in solidly converged predictions with almost similar convergence rates. Using similar Courant–Friedrichs–Lewy limits and grid sizes, the GO model required the least CPU time, followed by the SA and MM models, with differences of 3.3 and 4.4%, respectively. The MM and FS models had about the same difference of 6.0%, compared with the GO model. The WN model required the highest CPU time resulting in a difference of about 16.6%.

Flow over a Flat Plate at Zero Pressure Gradient

This case was one of the building bricks for testing the modifications and validating all other models for an equilibrium-flow test case. A good turbulence model should be capable of predicting the wall-law profile. The freestream Mach number was set to 0.3 and the Reynolds number was taken as 6.0×10^6. The flow was computed using an 81×81 grid with the first point off the wall, yielding a y^+ value of around 0.5. As expected, the present modifications do not alter the solution in equilibrium-flow cases; hence, the MM model yields good predictions for the flat-plate turbulent boundary layer. The comparison of all models results in the analytical wall-law profile given in Fig. 3. The computational profile was taken at 60% of the plate. The analytical wall-law profile was plotted according to $u^+ = y^+$ in the viscous sublayer, $u^+ = 5.0\,\ell_n(y^+) - 3.05$ in the buffer layer, and $u^+ = 2.5\,\ell_n(y^+) + 5.5$ in the logarithmic layer. The results of all models collapse very closely to the analytical solution, except for the GO model, which surprisingly underpredicts the logarithmic layer of the wall-law profile. The skin friction is plotted for the flat plate in Fig. 4. All models are compared with the empirical correlation by Schultz-Grunow, as reported in [23], $C_f/2 = 0.185/(\log_{10} Re_x)^{2.584}$. The skin-friction profile is very well predicted by all models.

Transonic Flow over the NACA 0012 Airfoil

A Mach 0.799 flow over the NACA 0012 airfoil with an angle of attack set at 2.26° and a Reynolds number of 9.0×10^6 was investigated. Experimental data for this case consist of wall pressure coefficient measurements along the upper and lower surfaces of the airfoil given by Harris [24]. This is one of the most challenging test cases, due to the shock-induced separation; hence, the sensitivity of the turbulence model is expected to be considerably more pronounced. The grid used had dimensions of 257×65, with 223 points lying on the airfoil surface. The first centroidal point in the offbody mesh was located at $y^+ \approx 1$. The far field was approximately extended to 16 chords from the airfoil surface. Figure 5 shows the surface pressure coefficient predicted by all models for the fully turbulent run. Overall, the MM model corresponds best to the experimental data in terms of the shock location and the postshock pressure coefficient profile. The GO model rates second at predicting the shock location and underpredicts the postshock behavior. The SA, ME, and FS models fall very close to each other, with the SA being the closest to the experimental shock location. The WN model rates last at predicting the shock location, which in turn indicates that the model predicted a delayed transition in the vicinity near the airfoil's leading edge. This behavior is clearly noted in the skin-friction coefficient over a flat plate, where the model predicts a deferred transition location when compared with all other models.

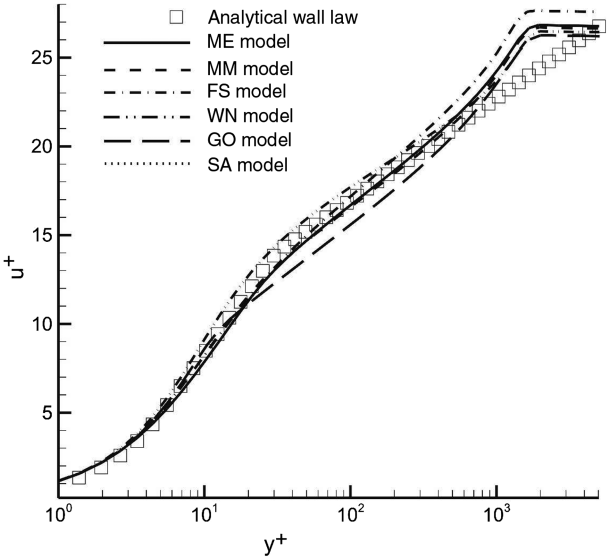

Fig. 3 Analytical law-of-the-wall profile for the flat-plate case.

Flow over the Aerospatiale-A Airfoil

The Aerospatiale-A airfoil is among the most challenging test cases, and relatively few computational studies have been carried out. The test case was computed on a 341×45 grid, with the first node off the surface at $y^+ \approx 2$. The airfoil's angle of attack was set at 13.3°

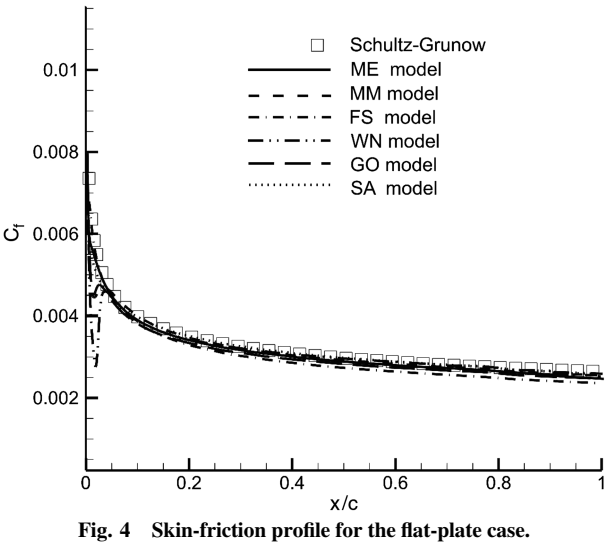

Fig. 4 Skin-friction profile for the flat-plate case.

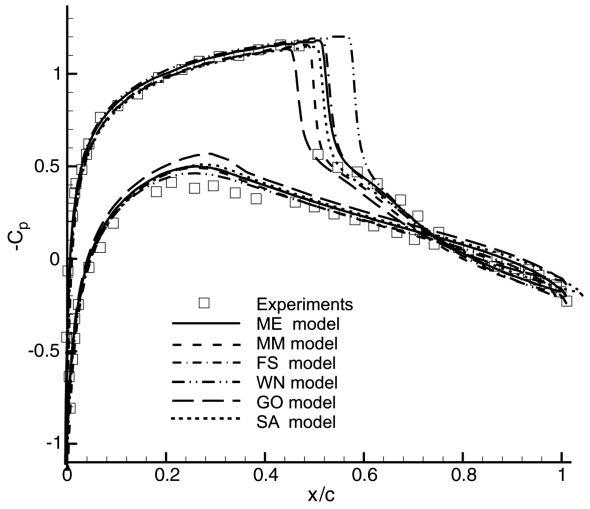

Fig. 5 Surface pressure distribution over the NACA 0012 airfoil.

with a Mach number and a Reynolds number of 0.2 and 2.0×10^6, respectively. Computations were performed by artificially tripping the boundary layer at 12 and 30% of the chord on the respective upper and lower surfaces of the airfoil. The skin-friction coefficient on the upper and lower sides of the airfoil is given in Fig. 6. The SA, FS, and MM models closely predict the experimental measurements, followed by the GO model, which slightly underpredicts the skin-friction coefficient distribution. The ME model shows the highest level of overprediction of the experimental measurements and is closely followed by the WN model, which seems to perform slightly better in the region close to the leading edge. A very mild laminar separation bubble is detected by all models on the suction side of the airfoil near $x/c = 0.1$, which is consistent with the experimental measurements [25]. Figure 7 shows the mean streamwise components of the normalized velocity profiles for the locations of $x/c = 0.3$, 0.7, 0.87, 0.96, and 0.99. The GO model returns the best prediction relative to all other models and is evident when inspecting velocity profiles located toward the trailing edge: specifically, at $x/c = 0.96$ and 0.99. The MM model rates second, followed by the SA model in near-wall regions and by the ME model away from the wall within the boundary layer. The velocity profiles predicted by the FS model fall on top of those predicted by the ME model in the vicinity of the wall and very close to those predicted by the WN model away from the wall. The WN model rates last at predicting velocity profiles on the suction side of the airfoil. It is worth mentioning that the SST model, which was assessed by Kotapati–Apparao et al. [26], did not produce qualitatively better results than those obtained by the GO and MM models.

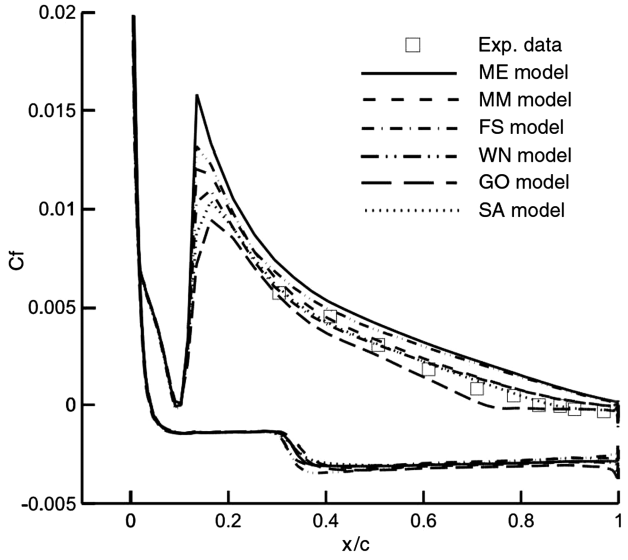

Fig. 6 Skin-friction coefficient distribution for the Aerospatiale-A airfoil.

Flow over the NACA 4412 Airfoil

The NACA 4412 is a challenging test case as it involves substantial separation and has been widely used in literature to validate turbulence models. The airfoil's high angle of attack, 13.87°, causes a large adverse pressure gradient on the suction side that rapidly thickens the boundary layer, leading to flow separation. The experimental data, which consists of velocity profiles at several locations along the suction side, is given by Coles and Wadcock [27]. The inflow Reynolds number was set to 1.52×10^6 with a Mach number of 0.2. A 257×91 grid was used with 191 nodes lying on the airfoil surface with a minimum wall distance of $y^+ \approx 1$ and an outer boundary extent of approximately 15 chords. The boundary layer was tripped at $x/c = 0.023$ and 0.1 along, respectively, the upper and lower surfaces of the airfoil. A comparison of the mean velocity profiles with the experimental measurements for all considered turbulence models are given in Fig. 8. The MM model correctly accounts for the nonequilibrium effects by accurately predicting the separation bubble height. In the near-wall region the SA model rates second at predicting the velocity profiles and the ME model outperforms the SA model at locations away from the wall. All models except the GO model predict velocities that are more consistent with the experimental data closer to the leading edge, but the discrepancies of the SA, ME, FS, and WN models magnify further downstream. The GO model rates last, as it well underpredicts

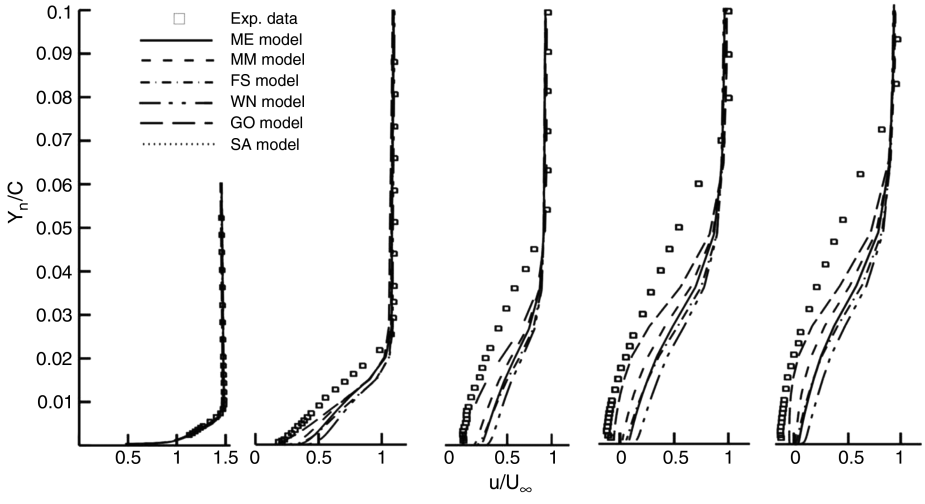

Fig. 7 Velocity profiles for the Aerospatiale-A airfoil at $x/c = 0.3$, 0.7, 0.87, 0.96, and 0.99 on the suction side of the airfoil.

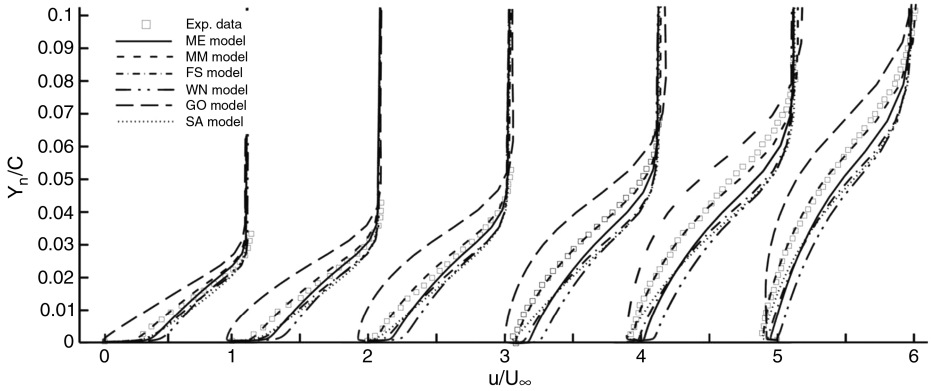

Fig. 8 Velocity profiles for NACA 4412 airfoil at $x/c = 0.675$, 0.731, 0.786, 0.842, 0.897, and 0.953 on the suction surface of airfoil.

the mean velocity profiles, followed by the WN model, which overpredicts these profiles and hence barely detects separation. The GO model predicts an early and a massive separation at $x/c = 0.602$ that falls well ahead of the experimental range [27] of $x/c=$ 0.75–0.8. This is followed by the SA model, which predicts separation within the range of $x/c = 0.75$–0.8. The MM and FS models predict separation at $x/c = 0.85$ and 0.86, respectively. Although the inclusion of the f_p function in the MM model results in the best velocity profiles, it does not seem to improve the model's capability of predicting the separation location. A delayed separation is predicted by both the ME and the WN models taking place at $x/c = 0.94$ and 0.97, respectively. Although both of these models incorporate different LRN terms and coefficients, the prediction of the separation point is fairly close and is downstream of the location predicted by the MM and the FS models. Thus, it may be concluded that the prediction of the separation point is mainly attributed to the form the destruction term. It is worth noting that the early separation predicted by the GO model, which responded too quickly to adverse pressure gradient, is mainly due to the destruction term that is similar to that of the BB model.

Backward-Facing-Step Flow

The final test case considered for evaluating the predictive capabilities of the six models is the Driver and Seegmiller [28] backward-facing-step flow test case. The Reynolds number based on the inlet velocity and the step height H was set to 37,500 with a Mach number of 0.128. The expansion ratio based on upstream to downstream channel heights was 1.125. This ratio is insufficient for pressure variation to overwhelm turbulence effects. The flow was computed using a grid size of 326×161 and extended from $x/H \approx -59$ upstream to $x/H \approx 40$ downstream of the step with a minimum wall distant of $y^+ \approx 0.17$. The original grid was used by Wilcox [14], extending only to $x/H \approx -4$ upstream of the step. The viscous adiabatic boundary condition was used on the lower wall and the back of the step. On the upper wall, a slip boundary condition was imposed toward the inlet of the channel, followed by a nonslip adiabatic boundary condition. This inviscid wall condition extended to $x/H \approx -34$ in order to match the experimental boundary-layer profile at $x/H \approx -4$ and the Reynolds number based on the momentum thickness, $Re_\theta = 5000$. At the inlet the pressure, velocities, and density were set to the freestream values, and the turbulent viscosity was extrapolated from the interior domain. At the outlet boundary, the pressure was set to $p/p_\infty = 1.005$, and all other flow variables were extrapolated from the interior domain. The lower-wall mean skin-friction coefficients for all six models are given in Fig. 9 and a close-up view of the entire recirculation region is given in Fig. 10. The reattachment length in the experiment was in the range of $l_r/H \approx 6.16$–6.36. The ME and SA models predicted the reattachment length within the range of 6.16 and 6.29, respectively. Both the WN and the FS models underestimated the reattachment length, predicting it at 5.68 and 5.49, respectively. The GO and the MM models overpredicted the reattachment length of the separation bubble with values of $l_r/H \approx 6.45$ and 6.51, respectively. The mean skin-friction coefficient downstream of the reattachment length is best predicted by the ME and the MM models, whereas the WN model overshoots near reattachment. This behavior is a result of low-Reynolds-number terms that the WN model carried on from the transformation of the low-Reynolds-number k-ε model. All other models underestimate the skin-friction coefficient downstream the

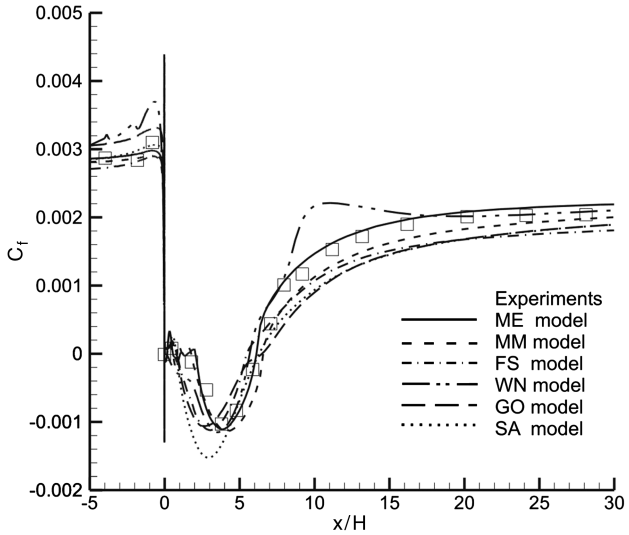

Fig. 9 Skin-friction coefficient distribution for the backward-facing step.

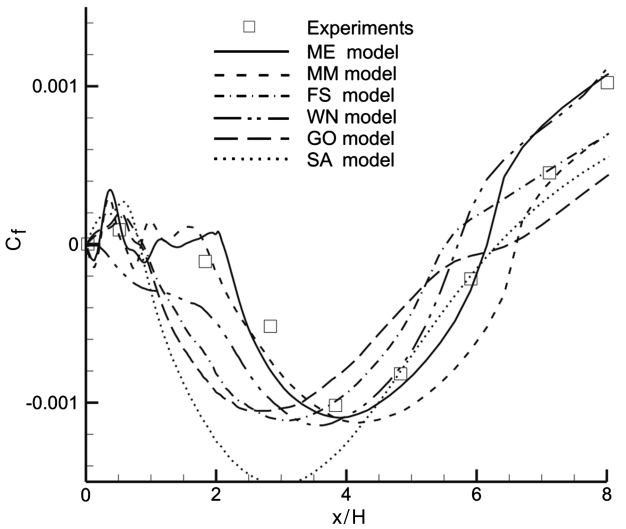

Fig. 10 Skin-friction coefficient distribution for the backward-facing step. A close-up view of the recirculation region.

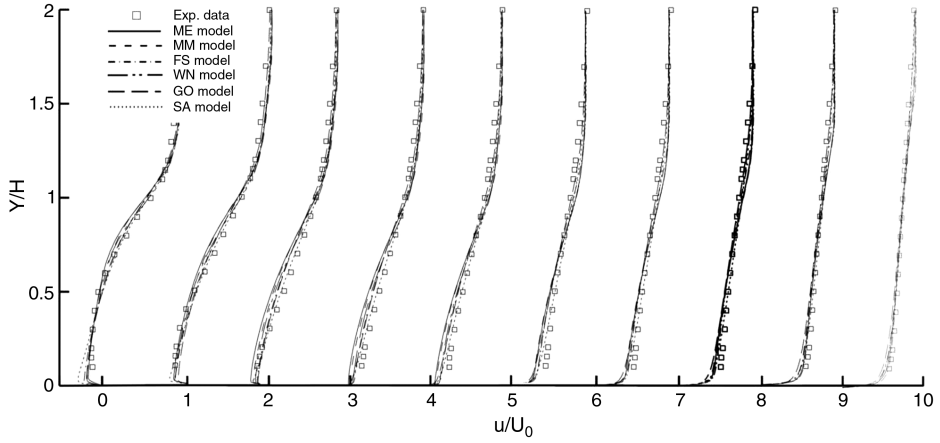

Fig. 11 Velocity profiles for the backward-facing step at $x/H = 2, 3, 5, 6, 7, 10, 12, 14, 20$, and 32 on the lower wall of the channel.

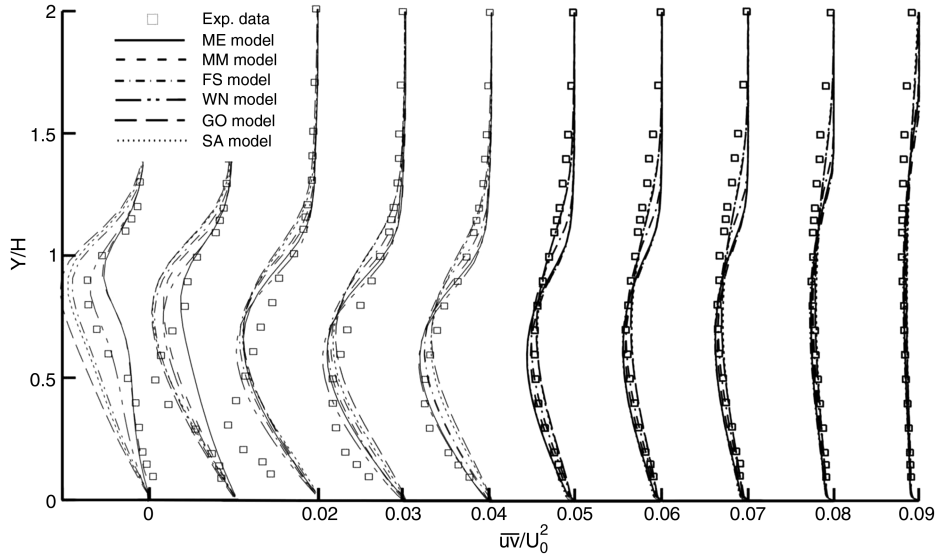

Fig. 12 Shear-stress profiles for the backward-facing step at $x/H = 2, 3, 5, 6, 7, 10, 12, 14, 20$, and 32 on the lower wall of the channel.

reattachment point. The SA model is not in good agreement in the separated region, as it underpredicts the experimental data, overshooting at around $x/H \approx 3$. The GO and FS models predict the depth of the separation zone at, respectively, $x/H \approx 2.5$ and 3 ahead of the experimental location. The ME and the MM models slightly underpredict the depth of the separation bubble, however, at nearly the same experimental location.

The velocity profiles for this test case are shown in Fig. 11. The results of all models are very similar, even in the recirculation region, and closely predict the experimental data. However, it appears that almost all models predict a sluggish recovery of velocity profiles, specifically, downstream of the reattachment point. Shear-stress profiles depicted in Fig. 12 show slight variation among models within the separation bubble and fall very close to each other downstream of the reattachment point. In the recirculation region, the WN model best predicts the shear-stress profiles, followed by the MM model. The latter shows a slight improvement when compared with the ME model. The SA and the GO models rate last, as they overpredict the shear-stress profiles close to the back of the step, at around $x/H \approx 2$ and 3, and underpredict them near the reattachment point, at around $x/H \approx 6$ and 7.

Conclusions

A study of one-equation turbulence models for several test flow cases has been conducted. These newly developed models, four of which are derived using Menter's methodology of transforming two-equation models, have been assessed against five different test cases. These flow cases ranged from a simple flat plate to highly nonequilibrium test cases that include flow separation and shock/boundary-layer interaction. The following conclusions are drawn from the study:

1) Generally, the MM model returns better predictions relative to all other models considered in this study. The modification of the destruction term did not deteriorate the performance of the model when qualitatively compared with its performance in a previous study; however, it rendered the model Galilean-invariant. For adverse-pressure-gradient flows the f_p function improves the predictive capability of the model in the outer part of the boundary layer; however, it has relatively no influence on the prediction of the separation point, which is mainly affected by the form of the destruction term.

2) The WN model sluggishly responds to adverse pressure gradient/shock/boundary-layer interaction flows and thus, is among the least suitable for such applications. The performance of this model, with a nonlocal formulation shortcoming, might be closely related to the transformation of the k-ε model, which encompasses the closure's LRN terms. The effect of these terms can be noted by the overshoot of the friction coefficient near the reattachment point in the backward-facing-step test case, a well-known behavior of k-ε model. Furthermore, it may be deduced that the models' calibration and LRN functions have stronger impact on the predictive capability of

the models in internal flow problems, compared with various forms of destruction terms.

3) The GO model violates the Galilean invariance and responds too strongly to adverse-pressure-gradient flows by predicting massive separation in attached regions. To a large extent, this behavior is related to the destruction term, which is similar to that of the BB model. Furthermore, the model is not properly calibrated, as it fails to predict the basic logarithmic-layer profile for the considered equilibrium flow over a flat plate.

4) The ME and the FS models' predictions are fairly close in all considered external-flow test cases. The latter better predicts separation in flows with adverse pressure gradient, whereas the former better performs in backward-facing-step internal channel flows. This is mainly due to the use of different destruction terms, as that of the FS model responds better to flows with adverse pressure gradients.

5) The SA model does a fair job of predicting internal and external flows. However, the model does not offer any advantage over other models, especially because it explicitly depends on the distance to the closest wall, rendering it less desirable in flowfields with complex geometries.

In future work, most of these models have to be applied to three-dimensional test cases to determine whether they are able to describe more complex engineering flowfields.

References

[1] Fröhlich, J., and Von Terzi, D., "Hybrid LES/RANS Methods for the Simulation of Turbulent Flows," *Progress in Aerospace Sciences*, Vol. 44, 2008, pp. 349–377. doi:10.1016/j.paerosci.2008.05.001

[2] König, D., Meinke, M., and Schröder, W., "Embedded LES-to-RANS Boundary in Zonal Simulations," *Journal of Turbulence*, Vol. 11, No. 7, 2010, pp. 1–25.

[3] Prandtl, L., "Über ein neues Formelsystem für die Ausgebildete Turbulentz," *Nachrichten der Akademie der Wissenschaften in Göttingen. II, Mathematisch-Physikalische Klasse*, 1945, pp. 6–19.

[4] Nee, V. W., and Kovasznay, L. S. G., "The Calculation of the Incompressible Turbulent Boundary Layer by a Simple Theory," *Physics of Fluids*, Vol. 12, 1968, pp. 473–484.

[5] Sekundov, A. N., "Application of a Differential Equation for Turbulent Viscosity to the Analysis of Plane Non-Self-Similar Flows," *Izvestiya Akademii Nauk SSSR, Mekhanika Zhidkosti i Gaza*, Vol. 5, Sept.–Oct. 1971, pp. 114–127.

[6] Baldwin, B., and Barth, T., "A One-Equation Turbulent Transport Model for High Reynolds Number Wall-Bounded Flows," NASA TM 102847, 1990.

[7] Menter, F. R., "Eddy Viscosity Transport Equations and Their Relation to the k-ε Model," *Journal of Fluids Engineering*, Vol. 119, 1997, pp. 876–884. doi:10.1115/1.2819511

[8] Spalart, P., and Allmaras, S., "A One-Equation Turbulence Model for Aerodynamic Flows," AIAA Paper 92-0439, 1992.

[9] Goldberg, U., "Hypersonic Flow Heat Transfer Prediction Using Single Equation Turbulence Models," *Journal of Heat Transfer*, Vol. 123, 2001, pp. 65–69. doi:10.1115/1.1337653

[10] Goldberg, U., "Turbulence Closure with a Topography-parameter-free Single Equation Model," *International Journal of Computational Fluid Dynamics*, Vol. 17, 2003, pp. 27–38. doi:10.1080/1061856031000083459

[11] Nagano, Y., Pei, C. Q., and Hattori, H., "A New Low-Reynolds-Number One-Equation Model of Turbulence," *Flow, Turbulence and Combustion*, Vol. 63, 2000, pp. 135–151. doi:10.1023/A:1009924002401

[12] Fares, E., and Schröder, W., "A General One-Equation Turbulence Model for Free Shear and Wall-Bounded Flows," *Flow, Turbulence and Combustion*, Vol. 73, 2005, pp. 187–215. doi:10.1007/s10494-005-8625-y

[13] Wu, X., and Nagano, Y., "A Simplified Low-Reynolds-Number One-Equation Model of Turbulence," *Proceedings of the 16th IASTED International Conference on Modelling and Simulation*, Cancun, Mexico, 18–20 May 2005.

[14] Wilcox, D. C., *Turbulence Modeling for CFD*, 2nd ed., DCW Industries, Inc., La Cãnada, CA, 2000.

[15] Elkhoury, M., "Assessment and Modification of One-Equation Models of Turbulence for Wall-Bounded Flows," *Journal of Fluids Engineering*, Vol. 129, 2007, pp. 921–928. doi:10.1115/1.2743666

[16] Elkhoury, M., "A Low-Reynolds-Number One-Equation Model of Turbulence," *The Aeronautical Journal*, Vol. 112, No. 1128, 2008, pp. 101–108.

[17] Mellor, G. L., and Herring, H. J., "Two Methods of Calculating Turbulent Boundary Layer Behavior Based on Numerical Solution of the Equation of Motion," *Computation of Turbulent Boundary Layers—1968 AFOSR-IFP-Stanford Conference Proceedings*, Stanford Univ., Thermosciences Div., Stanford, CA, 1968.

[18] Nagano, Y., and Tagawa, M., "An Improved k-ε Model for Boundary Layer Flows," *Journal of Fluids Engineering*, Vol. 112, 1990, pp. 33–39. doi:10.1115/1.2909365

[19] Durbin, P. A., Mansour, N. N., and Yang, Z., "Eddy Viscosity Transport Model for Turbulent Flow," *Physics of Fluids*, Vol. 6, 1994, pp. 1007–1015. doi:10.1063/1.868334

[20] Wilcox, D. C., "*Turbulence Modeling for CFD*," 3rd ed., DCW Industries, Inc., La Cãnada, CA, 2006.

[21] Ekaterinaris, J. A., Cricelli, A., and Platzer, M. F., "A Zonal Method for Unsteady Viscous, Compressible Airfoil Flows," *Journal of Fluids and Structures*, Vol. 8, 1994, pp. 107–123. doi:10.1006/jfls.1994.1005

[22] Rai, M. M., and Chakravarthy, S. R., "An Implicit Form of the Osher Upwind Scheme," *AIAA Journal*, Vol. 24, 1986, pp. 735–743. doi:10.2514/3.9340

[23] Schlichting, H., "*Boundary Layer Theory*," McGraw–Hill, New York, 1979.

[24] Harris, C., "Two-Dimensional Aerodynamic Characteristics of the NASA 0012 Airfoil in the Langley 8-Foot Transonic Pressure Tunnel," NASA TM-81927, 1981.

[25] Mellen, C. P., Fröhlich, J., and Rodi, W., "Lessons from the European LESFOIL Project on LES of Flow Around an Airfoil," AIAA Paper 2002-0111, 2002.

[26] Kotapati–Apparao, R., Squires, K. D., and Forsythe, J. R., "Prediction of the Flow over an Airfoil at Maximum Lift," AIAA Paper No. 2004-0259, 2004.

[27] Coles, D., and Wadcock, A. J., "Flying Hot Wire Study of Flow Past an NACA 4412 Airfoil at Maximum Lift," *AIAA Journal*, Vol. 17, 1979, pp. 321–328. doi:10.2514/3.61127

[28] Driver, D. M., and Seegmiller, H. L., "Features of a Reattaching Turbulent Shear Layer in Divergent Channel Flow," *AIAA Journal*, Vol. 23, No. 2, 1985, pp. 163–171. doi:10.2514/3.8890

F. Ladeinde
Associate Editor